ELSEVIER

Journal of Power Sources 106 (2002) 284–294

JOURNAL OF POWER SOURCES

www.elsevier.com/locate/jpowsour

Three-dimensional computational analysis of transport phenomena in a PEM fuel cell

T. Berning[a], D.M. Lu[b], N. Djilali[a,*]

[a]*Institute for Integrated Energy Systems, University of Victoria, Victoria, Canada*
[b]*Trojan Technologies, London, Ont., Canada*

Abstract

A comprehensive non-isothermal, three-dimensional computational model of a polymer electrolyte membrane (PEM) fuel cell has been developed. The model incorporates a complete cell with both the membrane-electrode-assembly (MEA) and the gas distribution flow channels. With the exception of phase change, the model accounts for all major transport phenomena.

The model is implemented into a computational fluid dynamics code, and simulations are presented with an emphasis on the physical insight and fundamental understanding afforded by the detailed three-dimensional distributions of reactant concentrations, current densities, temperature and water fluxes. The results show that significant temperature gradients exist within the cell, with temperature differences of several degrees K within the MEA. The three-dimensional nature of the transport is particularly pronounced under the collector plates land area and has a major impact on the current distribution and predicted limiting current density.

Keywords: PEM fuel cells; PEFC; Fuel cell modelling; CFD

1. Introduction

Fuel cells convert the chemical energy of hydrogen and oxygen directly into electricity. Their high efficiency and low emissions have made them a prime candidate for powering the next generation of electric vehicles, and their modular design and the prospects of micro-scaling them have gained the attention of cellular phone and laptop manufacturers. Their scalability and relative flexibility in terms of fuel makes them prime candidates for a variety of stationary applications including distributed residential power generation. The basic structure and operation principle of the polymer electrolyte membrane (PEM) fuel cell considered here are illustrated in Fig. 1.

The polymer electrolyte consists of a perfluorinated polymer backbone with sulfonic acid side chains. When fully humidified, this material becomes an excellent protonic conductor. The membrane, the catalyst (platinum supported on carbon particle) and the two electrodes (teflonated porous carbon paper or cloth) are assembled into a sandwich structure to form a membrane-electrode-assembly (MEA). The MEA is placed between two graphite bipolar plates with machined groves that provide flow channels for distributing the fuel (hydrogen) and oxidant (oxygen from air).

The hydrogen rich fuel fed to the anode side diffuses through the porous gas-diffusion electrode (GDE). At the catalyst layer, the hydrogen splits into hydrogen protons and electrons according to:

$$2H_2 \Rightarrow 4H^+ + 4e^- \quad (1)$$

Driven by an electric field, the H^+ ions migrate through the polymer electrolyte membrane. The oxygen in the cathode gas stream diffuses through the towards the catalyst interface where it combines with the hydrogen protons and the electrons to form water according to:

$$O_2 + 4H^+ + 4e^- \Rightarrow 2H_2O \quad (2)$$

The overall reaction is exothermic and can be written as:

$$2H_2 + O_2 \Rightarrow 2H_2O + \text{electricity} + \text{heat} \quad (3)$$

Several coupled fluid flow, heat and mass transport processes occur in a fuel cell in conjunction with the electrochemical reaction. These processes have a significant impact on two important operational issues: (i) thermal and water management; (ii) mass transport limitations. Water management ensures that the PEM remains fully hydrated to maintain good ionic conductivity and performance. Water content of the membrane is determined by the balance between water production and three water transport processes: electro-osmotic drag of water, associated with proton migration through the membrane from the anode to the cathode side;

* Corresponding author. Tel.: +1-250-7216034; fax: +1-250-7216051.
E-mail address: ndjilali@uvic.ca (N. Djilali).

0378-7753/02/$ – see front matter
PII: S0378-7753(01)01057-6

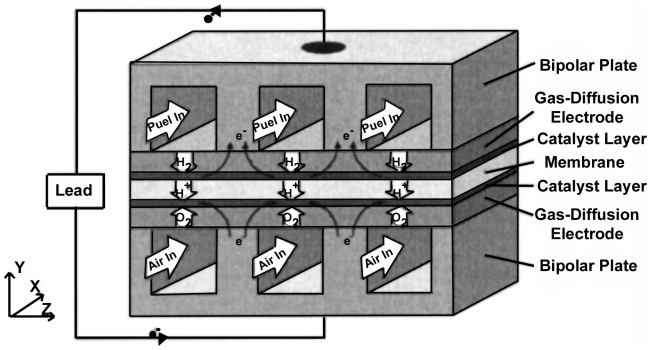

Fig. 1. Schematic of a PEM fuel cell.

back diffusion from the cathode; and diffusion of water to/from the oxidant/fuel gas streams. Without control, an imbalance between production and removal rates of water can occur. This results in either dehydration of the membrane, or flooding of the electrodes; both phenomena have a very detrimental effect on performance and fuel cells have to be carefully designed to avoid the occurrence of either phenomenon. Thermal management is required to remove the heat produced by the electrochemical reaction (up to ~50% of the energy produced during high power density operation) in order to prevent drying out of the membrane and excessive thermal stresses that may result in rupture of the membrane. The small temperature differentials between the fuel cell stack and the operating environment make thermal management a challenging problem in PEMFCs.

Because of the highly reactive environment of a fuel cell it is not possible to perform detailed in situ measurements during operation. Such information has been sought through modelling and simulation in order to improve understanding of water and species transport, optimize thermal management and shorten the design and optimization cycles. Modelling of fuel cells is challenging, because the processes involve multi-component, multi-phase, and multi-dimensional flow, heat and mass transfer with electrochemical reactions, all occurring in irregular geometries including porous media. Numerous authors have developed fuel cell models accounting for various physical processes. The most prominent earlier works stem from Bernardi and Verbrugge [3,4] and Springer et. al. [14], who developed one-dimensional, isothermal models of the MEA. Fuller and Newman [8] published a quasi two-dimensional model based on concentration theory. The work by Nguyen and White [12], and Yi and Nguyen [21] was two-dimensional in nature, but the GDEs were omitted, assuming "ultrathin" electrodes. The importance of accounting for temperature gradients in fuel cells modelling was demonstrated in the work of Woehr et. al. [20] and Djilali and Lu [7]. The important issue of water flooding was addressed by Baschuk and Li in a recent one-dimensional model [2].

Earlier models were primarily analytic and required a number of simplifications due to the limitations of the numerical techniques. More recently, a general trend can be observed to apply the methods of computational fluid dynamics to fuel cell modelling. Gurau et al. [9] published a fully two-dimensional model of a whole fuel cell, i.e. two gas-flow channels separated by the MEA. Um et al. [18] and Wang et al. [19] have developed a similar model and included two phase flow. However, the underlying assumption was isothermal behaviour, which is a serious modelling limitation as we will see later. The local temperature distribution has a significant impact on the amount of water that undergoes phase change, and therefore the isothermal assumption can lead to results that are not physically representative when phase change is accounted for. Finally as a result of the architecture of a cell, the transport phenomena in a fuel cell are inherently three-dimensional, but no models have yet been published to address this.

In this paper we address simultaneously the need to account for thermal gradients and multi-dimensional transport using a computational fluid dynamics based approach that couples convective transport in the gas-flow channels with transport and electrochemistry in the MEA.

2. Model description

The PEM fuel cell model presented here is a comprehensive three-dimensional, non-isothermal, steady-state model providing a detailed description of the following transport phenomena:

- multi-component flow;
- convective heat and mass transport in the flow channels;
- diffusion of reactants through porous electrodes;
- electrochemical reactions;
- migration of H^+ protons through the membrane;
- transport of water through the membrane;
- transport of electrons through solid matrix;
- conjugate heat transfer.

The equations governing these processes include the full mass and momentum conservation equations (Navier–Stokes equations) governing fluid flow, the species conservation and energy equations and four additional phenomenological equations tailored to account for processes specific to fuel cells [3]:

- the Stefan–Maxwell equations for multi-species diffusion;
- the Nernst–Planck equation for the transport of protons through the membrane;
- the Butler–Volmer equation for electrochemical kinetics and;
- the Schlögl equation for the transport of liquid water through the membrane.

These equations and appropriate boundary conditions were implemented in their three-dimensional form into

the commercial computational fluid dynamics code CFX-4.3 (AEA Technology); the implementation required the development of an extensive suite of user subroutines. Customized iterative procedures were also implemented to ensure effective coupling between the electrochemistry and the fluid transport processes.

2.1. Model assumptions

A complete fuel cell is an extremely complex system involving both microscale and macroscale geometric features and transport processes. In order to devise a numerically tractable three-dimensional model of a complete cell it is necessary to invoke a number of simplifying assumptions. The most important ones are:

(1) the fuel cell operates under steady-state conditions;
(2) all gases are assumed to be compressible ideal gases, fully saturated with water vapour;
(3) the flow in the channels is considered laminar;
(4) the membrane is assumed to be fully humidified so that the electronic conductivity is constant and no diffusive terms have to be considered for the liquid water flux;
(5) since it was determined in an earlier study [4] that cross-over of reactant gases can be neglected, the membrane is currently considered impermeable for the gas phase;
(6) the water in the pores of the diffusion layer is considered separate from the gases in the diffusion layers, i.e. no interaction between the gases and the liquid water exists;
(7) the product water is assumed to be in the liquid phase;
(8) Ohmic heating in the collector plates and in the GDEs is neglected due to their high conductivity;
(9) heat transfer inside the membrane is accomplished by conduction only, i.e. the enthalpy carried by the net movement of liquid water is currently neglected;
(10) the catalyst layer is assumed to be a thin interface where sink and source terms for the reactants and enthalpy are specified;
(11) electroneutrality prevails inside the membrane. The proton concentration in the ionomer is assumed to be constant and equal to the concentration of the fixed sulfonic acid groups.

Most of the above assumptions are a ''standard'' feature of almost all previous modelling studies. In addition, commonly used assumptions in previous studies were: (i) one or two-dimensionality; (ii) de-coupling of MEA and flow channel transport; (iii) isothermal conditions. In the present model these limiting assumptions are removed. One of the other major limitations, namely the assumption of a single phase and of non-interacting water and gas phases in the pores of the GDEs will be addressed in future work with the implementation of a two-phase model with both phases interacting in the same computational domain.

2.2. Modelling domain and geometry

The computational domain that was employed for the simulations is shown in Fig. 2. In addition to transport across the MEA (y-direction), the formulation allows us to account for and investigate the effect of non-uniform transfer rates and species concentration along the flow channels (x-direction), as well as the three-dimensional effects in the transverse z-direction due to the geometry (alternating open flow channels with land areas). These effects are expected to be particularly important in the regions of the GDEs under the collector plates and not directly exposed to the flow fields. We take advantage of the geometric periodicity of the cell in order to reduce the size of the computational domain and hence computational cost. Symmetry is therefore assumed in the middle planes of the flow channel and land areas and hence only half of each needs to be incorporated in the domain. This is a valid assumption as long as no cross-flow takes place between adjacent channels, as in inter-digitated designs, and as long as the region considered consists of parallel straight channels, as is the case for the bulk of the collector plates of an actual fuel cell.

In order to effectively implement the numerical solution of the various transport equations, three subdomains were defined within the main computational domain.

- The main domain accounts for the flow, heat and mass transfer of the reactant gases inside the flow channels and the GDEs.
- Subdomain I consists of the MEA only, and accounts for the heat flux through the solid matrix of the GDEs and the membrane. Hence, the only variable of interest here is the temperature. Exchange terms between this subdomain and Domain I account for the heat transfer between the solid phase and the gas phase.
- Subdomain II is used to solve for the flux of liquid water through the MEA. The flux of the water in the membrane is coupled to the electrical potential calculated in Domain III via the Schlögl equation.
- Subdomain III consists of the membrane only and is used to calculate the electrical potential inside the membrane.

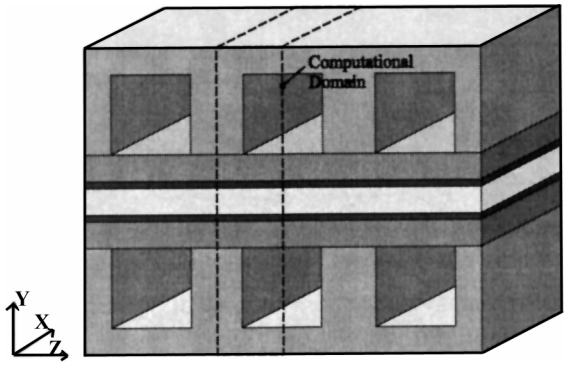

Fig. 2. Three-dimensional computational domain.

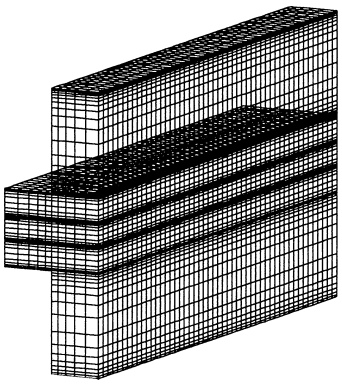

Fig. 3. Computational mesh for the MEA and gas-flow channel regions. The "empty" blocks on the left corresponds to the bipolar plates, which have been left out for clarity.

The main domain and three subdomains are all coupled through appropriate boundary exchange terms and an iterative solution procedure. The computational mesh is shown in Fig. 3. Due to the large number of coupled equations that are solved and the overall complexity of the problem, the number of computational cells was limited to roughly 80,000. The calculations presented here have all been obtained on a PC with a 450 MHz Pentium II. The number of iterations required to obtain converged solutions ranged from 2000 for lower current densities to 20,000 for higher current densities; the latter required about 50 h of CPU time.

2.3. Model equations

2.3.1. Notation

In the following, the subscript "g" denotes properties of the gas phase, whereas "l" stands for the liquid phase and "s" for the solid phase. Different species are denoted by the subscript "*i*", i.e. the subscript "g*i*" denotes the species "*i*" in the gas phase. "w" is used for water (species), "sat" means saturation value. Cathode side and anode side properties are denoted by the subscripts "c" and "a", respectively.

2.3.2. Fuel cell channels

In the fuel cell channels, the gas-flow field is obtained by solving the steady-state Navier–Stokes equations, i.e. the continuity equation:

$$\nabla \cdot (\rho_g \boldsymbol{u}_g) = 0 \tag{4}$$

and momentum equation

$$\nabla \cdot (\rho_g \boldsymbol{u}_g \otimes \boldsymbol{u}_g - \mu_g \nabla \boldsymbol{u}_g) = -\nabla \cdot (p + \tfrac{2}{3}\mu_g \nabla \cdot \boldsymbol{u}_g) + \nabla \cdot [\mu_g (\nabla \boldsymbol{u}_g)^T] \tag{5}$$

The temperature field is obtained by solving the convective energy equation

$$\nabla \cdot (\rho_g \boldsymbol{u}_g H_g - \lambda_g \nabla T_g) = 0 \tag{6}$$

here ρ_g is the gas phase density, $\boldsymbol{u} = (u, v, w)$ the fluid velocity vector, p the pressure, T the temperature, μ is the molecular viscosity and λ is the thermal conductivity.

The total enthalpy H is determined from the static (thermodynamic) enthalpy h via:

$$H_g = h_g + \tfrac{1}{2}\boldsymbol{u}_g^2 \tag{7}$$

where the bulk enthalpy is related to the mass fraction y and the enthalpy of each gas by:

$$h_g = \sum y_{gi} h_{gi} \tag{8}$$

The mass fraction of the different species obeys a transport equation of the same form as the generic advection-diffusion equation:

$$\nabla \cdot (\rho_g \boldsymbol{u}_g y_{gi}) - \nabla \cdot (\rho_g D_{gi} \nabla y_{gi}) = S_{gi} \tag{9}$$

where the i represents oxygen at the cathode side and hydrogen at the anode side and D_{gi} is the diffusivity of the species in the background fluid. The source term S_{gi} is determined by solving the Stefan–Maxwell equations, which account for the diffusion of multiple species [15]:

$$\nabla \cdot x_{gi} = \sum \frac{x_{gi} x_{gj}}{D_{ij}} (\boldsymbol{v}_i - \boldsymbol{v}_j) \tag{10}$$

where $\boldsymbol{v}_i$ is the diffusion velocity vector of species i, x the molar fraction and D_{ij} the binary diffusivity of any two species.

The second species on both sides is water vapour, which is assumed to exist at the saturation pressure, so that the molar fraction of water vapour is given by

$$x_{gw} = \frac{p_w^{sat}(T)}{p_g} \tag{11}$$

The saturation pressure of water vapour has been approximated by [14]

$$\log_{10} p_w^{sat}(T) = -2.1794 + 0.02953T - 9.1837T^2 + 1.4454T^3 \tag{12}$$

where T is the temperature in K. The mass fraction is related to the molar fraction by

$$y_{gi} = \frac{x_{gi} M_i}{\sum x_{gi} M_i} \tag{13}$$

where M is the molecular weight of the different species.

The ideal gas assumption leads to

$$\rho_{gi} = \frac{p_g M_i}{RT} \tag{14}$$

and the bulk density becomes:

$$\frac{1}{\rho_g} = \sum \frac{y_{gi}}{\rho_{gi}} \tag{15}$$

The sum of all mass fractions is equal to unity

$$\sum y_{gi} = 1 \tag{16}$$

which determines the mass fraction of the third species on both sides (nitrogen at the cathode and carbon dioxide at the anode).

2.3.3. Gas diffusion electrodes

In the porous GDEs the Navier–Stokes equations have to be corrected for the porosity ε of the carbon fiber paper. Thus, the conservation equation for mass becomes

$$\nabla \cdot (\rho_g \varepsilon_g \boldsymbol{u}_g) = 0 \tag{17}$$

whereas the momentum equation reduces to Darcy's law:

$$\varepsilon_g \boldsymbol{u}_g = -\frac{k_p}{\mu_g} \nabla p_g \tag{18}$$

where k_p denotes the hydraulic permeability. It was mentioned earlier that the liquid water pores are de-coupled from the gas pores, and Darcy's law is again used for liquid water transport:

$$\varepsilon_l \boldsymbol{u}_l = -\frac{k_p}{\mu_l} \nabla p_l \tag{19}$$

The mass transport equation in porous media becomes

$$\nabla \cdot (\rho_g \varepsilon_g \boldsymbol{u}_g y_{gi}) - \nabla \cdot (\rho_g D_{gi} \varepsilon_g \nabla y_{gi}) = S_{gi} \tag{20}$$

and the Stefan–Maxwell equations remain the same:

$$\nabla \cdot x_{gi} = \sum \frac{x_{gi} x_{gj}}{D_{ij}^{\text{eff}}} (\boldsymbol{v}_i - \boldsymbol{v}_j) \tag{21}$$

where the binary diffusivities D_{ij}^{eff} have been corrected for the porosity. This was done by applying the so-called Bruggemann correction:

$$D_{ij}^{\text{eff}} = D_{ij} * \varepsilon_g^{1.5} \tag{22}$$

Finally, the energy equation in the diffusion layer is given by

$$\nabla \cdot (\rho_g \varepsilon_g \boldsymbol{u}_g H_g - \lambda_g \nabla T_g) = \varepsilon_g \beta (T_g - T_s) \tag{23}$$

where the term on the right hand side accounts for the heat transfer from the solid matrix to the gas phase. β is a modified heat transfer coefficient that accounts for the convective heat transfer in W/m^2 and the specific surface area m^2/m^3 of the porous medium. Hence, the unit of β is [W/m^3].

In the solid matrix of the gas-diffusion layer, heat transfer is calculated via:

$$\nabla \cdot (\lambda_s \nabla T_s) = \varepsilon_g \beta (T_s - T_g) \tag{24}$$

2.3.4. Catalyst layer

As mentioned before, the catalyst layer is treated as a thin interface, where sink and source terms for the reactants are implemented. Due to the infinitesimal thickness, the source terms are actually implemented in the last grid cell of the porous medium. At the cathode side, the sink term for oxygen is given by

$$S_{O_2} = -\frac{M_{O_2}}{4F} i_c \tag{25}$$

whereas the sink term for hydrogen is specified as

$$S_{H_2} = -\frac{M_{H_2}}{2F} i_a \tag{26}$$

where F is the Faraday constant (96487 C/mol) and i is the local current density. Again, M is the molecular weight of the species i. The product water is assumed to be in liquid form, and hence the source term can be written as

$$S_{H_2O_{(l)}} = \frac{M_{H_2O}}{2F} i_c \tag{27}$$

The generation of heat in the cell is due to entropy changes as well as irreversibilities due to the activation overpotential η_{act} [11]:

$$\dot{q}_c = \left[\frac{T(-\Delta S_c)}{n_{e^-} F} + \eta_{\text{act}} \right] i_c \tag{28}$$

where T is the temperature, ΔS_c is the entropy change in the chemical reactions, n_{e^-} is the number of electrons transferred and η_{act} is the activation overpotential. Because both these contributions are small at the anode side, the source term is currently neglected here. The overpotential η_{act} can be estimated a priori. This does not introduce a large error, since the range of the activation overpotential at the cathode side is well known, depending on the catalyst loading and the expected exchange current density.

As can be seen from Eqs. (25)–(28), for an accurate solution of the reactant gas distribution inside the fuel cell, it is crucial to obtain the local current density distribution i, which is described by the Butler–Volmer equation [1]:

$$i_c = i_0^{\text{ref}} \left(\frac{c_{O_2}}{c_{O_2}^{\text{ref}}} \right) \left[\exp\left(\frac{\alpha_a F}{RT} \eta_{\text{act}} \right) - \exp\left(-\frac{\alpha_c F}{RT} \eta_{\text{act}} \right) \right] \tag{29}$$

and

$$i_a = i_0^{\text{ref}} \left(\frac{c_{H_2}}{c_{H_2}^{\text{ref}}} \right)^{1/2} \left[\exp\left(\frac{\alpha_a F}{RT} \eta_{\text{act}} \right) - \exp\left(-\frac{\alpha_c F}{RT} \eta_{\text{act}} \right) \right] \tag{30}$$

where c denotes the concentration of the reactants, and α_a and α_c are the so-called transfer coefficients. The reference exchange current density i_0^{ref} depends on various parameters such as operating temperature and catalyst loading, and a number of experiments have been conducted to quantify this dependence empirically [13,16].

2.3.5. Membrane model

In the membrane, the model accounts for the flux of liquid water and the protonic flux together with the distribution of electrical potential Φ are being considered. The transport of liquid water through the membrane is governed by a modified version of Darcy's law, the Schlögl equation [3]:

$$\boldsymbol{u}_l = \frac{k_\phi}{\mu_l} z_f c_f F \cdot \nabla \Phi - \frac{k_p}{\mu_l} \cdot \nabla p \tag{31}$$

where k_ϕ denotes the hydraulic permeability, z_f is the fixed-charge number in the membrane, c_f is the fixed-charge concentration and μ_l is the liquid water viscosity. This equation accounts for two different water transport processes: the electro-osmotic drag whereby hydrogen protons migrating through the membrane drag water molecules with them, and pressure driven flux, which is usually directed from the cathode side to the anode side. Strictly speaking, a diffusive term has to be accounted for as well, since the back diffusion of water can play an important role for water management schemes. However, when the membrane is fully humidified, as is assumed here, this term drops.

Heat transfer in the membrane is governed by

$$\nabla\lambda_{\text{mem}} \cdot \nabla T = \frac{i^2}{\kappa} \tag{32}$$

where κ is the electric resistance of the membrane material. Note that this implies that the transport of energy by the liquid water is neglected and the membrane is considered as a heat-conducting solid. The term on the right hand side of the equation denotes Ohmic heating inside the membrane. The local current density inside the membrane is obtained from Ohm's law:

$$i = -\kappa\nabla\Phi \tag{33}$$

Finally, for the electrical potential in the membrane, it can be shown that for a fully hydrated membrane it is governed by the Laplace equation [4]:

$$\nabla^2\Phi = 0 \tag{34}$$

2.3.6. Bipolar plates

Bipolar plates serve to transfer the electrons and separate different cells. Since the electrical conductivity of graphite λ_{gr} is high, Ohmic losses are neglected, and the energy equation reduces to

$$\nabla\lambda_{\text{gr}} \cdot \nabla T = 0 \tag{35}$$

2.3.7. Cell potential

The cell potential E is obtained by substracting all overpotentials (losses) from the equilibrium potential, i.e.

$$E = E^0_{T,p} - \eta_{\text{act}} - \eta_\Omega - \eta_{\text{mem}} \tag{36}$$

where $E^0_{T,p}$ is the equilibrium potential for a given temperature and pressure, η_{act} the activation overpotential at both sides, η_Ω are the Ohmic losses in the GDE plus contact resistances and η_{mem} is the Ohmic loss in the membrane.

The equilibrium potential $E^0_{T,p}$ is a function of pressure and temperature and is determined using the Nernst law [5],

$$E^0_{T,p} = E^0 + \frac{\Delta S}{nF}(T - T^0) + \frac{RT}{nF}\left[\ln p_{\text{H}_2} + \frac{1}{2}\ln p_{\text{O}_2}\right] \tag{37}$$

where p denotes the partial pressure of the species, n is the number of electrons transferred in the reaction, and ΔS is the change in entropy. The standard reversible potential E^0 is given by [5]

$$E^0 = \frac{\Delta G^0}{nF} \tag{38}$$

where ΔG^0 is the change in the standard Gibbs free energy of the reaction. Using standard values for the entropy production, Eq. (37) yields [2]

$$E^0_{T,p} = 1.229 - 0.83 \times 10^{-3}(T - 298.15) + \times 4.31 \times 10^{-5} T\left[\ln p_{\text{H}_2} + \frac{1}{2}\ln p_{\text{O}_2}\right] \tag{39}$$

2.4. Boundary conditions

Boundary conditions have to be applied for all variables of interest in each computational domain. In order to reduce computational cost, we take advantage of the geometric periodicity of the cell. Hence symmetry is assumed in the z-direction, i.e. all gradients in the z-direction are set to zero at the x–y plane boundaries of the domain. With the exception the channel inlets and outlets, a zero flux condition is applied at all x-boundaries (y–z planes).

The inlet values at the anode and cathode are prescribed for the velocity, temperature and species concentrations (Dirichlet boundary conditions). The inlet velocity is a function of the desired average current density i_{ave}, the geometrical area of the membrane A_{MEA}, the channel cross-section area A_{ch}, and the stoichiometric flow ratio ζ, according to:

$$u_{\text{in,c}} = \zeta_{\text{c}} \frac{i_{\text{ave}}}{4F} A_{\text{MEA}} \frac{1}{x_{\text{O}_2,\text{in}}} \frac{RT_{\text{in,c}}}{p_{\text{c,in}}} \frac{1}{A_{\text{ch}}} \tag{40}$$

and

$$u_{\text{in,a}} = \zeta_{\text{a}} \frac{i_{\text{ave}}}{2F} A_{\text{MEA}} \frac{1}{x_{\text{H}_2,\text{in}}} \frac{RT_{\text{in,a}}}{p_{\text{a,in}}} \frac{1}{A_{\text{ch}}} \tag{41}$$

where R is the universal gas constant, T_{in} is the inlet temperature and p_{in} is the inlet pressure.

At the outlets of the gas-flow channels, only the pressure is being prescribed as the desired electrode pressure; for all other variables, the gradient in the flow direction (x) is assumed to be zero (Neumann boundary conditions).

Since the fluid channels are bordered by the collector plates, no boundary conditions have to be prescribed here and conjugate heat transfer, impermeability and no-slip conditions are implemented implicitly at solid–fluid interfaces within the domain. At the outer boundaries of the bipolar plates (y-direction), boundary conditions need only to be given for the energy equation. This can be done by prescribing the heat flux or the temperature distribution. In the present simulations a zero heat flux condition was used, $\partial T/\partial y = 0$. This is not an entirely physical condition, but is adequate for the present simulations in which the focus is on model validation and identification of key transport

processes. In future work we intend to implement a cooling flow channel in the computational domain to remove arbitrary specification of the heat flux or temperature.

2.4.1. Subdomain I

As discussed earlier, three subdomains are defined for numerical efficiency. Subdomain I is used to solve for the heat flux through the solid matrix of the porous GDE. The only variable of interest here is the temperature, and it is assumed that all the heat transfer takes place to and from the gas phase inside the porous medium only. Adiabatic boundary conditions are therefore applied at all boundaries of this domain

$$\frac{\partial T}{\partial n} = 0 \tag{42}$$

2.4.2. Subdomain II

For the liquid water transport through the MEA in Subdomain II, the pressure is given at the outer boundaries of the GDE, i.e. the channel/GDE interface

$$P_{\mathrm{a,l}} = 3\,\mathrm{atm} \tag{43}$$

and

$$P_{\mathrm{c,l}} = 5\,\mathrm{atm} \tag{44}$$

Table 1
Geometrical, operational, electrode and membrane parameters for the base case

Property	Value
Channel length, l	0.05 m
Channel height, h	1.0×10^{-3} m
Channel width, w_c	1.0×10^{-3} m
Land area width, w_l	1.0×10^{-3} m
Electrode thickness, t_e	0.26×10^{-3} m
Membrane thickness, t_{mem}	0.23×10^{-3} m
Inlet fuel and air temperature, T_{in}	80 °C
Air side pressure, p_c	5 atm
Fuel side pressure, p_a	3 atm
Air stoichiometric flow ratio, ζ_c	3
Fuel stoichiometric flow ratio, ζ_a	3
Relative humidity of inlet gases, ξ	100%
Oxygen/nitrogen ratio, ψ	0.79/0.21
Gas phase electrode porosity, ε_g	0.4 [4]
Electronic conductivity, σ	6000 S/m
Effective thermal conductivity, λ_{eff}	75 W/mK [9]
Heat transfer coefficient between solid and gas phase, β	7.0×10^{5} W/m^3
Transfer coefficient, anode side, α_a	0.5
Transfer coefficient, cathode side, α_c	1 [17]
Ref. exchange current density, anode, $i_{0,a}^{ref}$	0.6 A/cm^2
Ref. exchange current density, cathode, $i_{0,c}^{ref}$	4.4×10^{-7} A/cm^2
Entropy change of cathode side reaction, ΔS_{Pt}	−326.36 J/(mol K) [11]
Ionic conductivity of the membrane, κ	0.06 S/cm
Protonic diffusion coefficient, D_{H^+}	4.5×10^{-9} m^2/s^2 [4]
Fixed-charge concentration, c_f	1200 mole/m^3 [4]
Fixed-site charge, z_f	−1
Electrokinetic permeability, k_ϕ	2.0×10^{-20} m^2 [4]
Hydraulic permeability, k_p	1.8×10^{-18} m^2 [4]
Thermal conductivity of the membrane, λ	0.67 W/mK [10]

At the interfaces exposed to the land area, no-flux conditions are imposed.

2.4.3. Subdomain III

Finally, for the membrane domain, where the only variable of interest is the electric potential, a reference potential value of zero is arbitrarily set at the anode side

$$\Phi = 0 \tag{45}$$

and at the cathode side, the potential distribution at the membrane/catalyst interface is computed from [4]

$$\frac{\partial \Phi}{\partial y} = -\frac{1}{\kappa_{\mathrm{eff}}}\left[i - Fc_{\mathrm{f}}\nu\varepsilon_{\mathrm{l,mem}}\right] \tag{46}$$

2.5. Modelling parameters

The parameters used for the base case simulations presented here are shown in Table 1. Since the model presented here was initially developed by extending the formulation of Bernardi and Verbrugge [3,4] to three-dimensions, many of the key parameters defined by these authors are still used here. It is important to note that because this model accounts for all major transport processes and the modelling domain comprises all the elements of a complete cell, no parameters needed to be adjusted in order to obtain physical results. When comparing our results with experiments published in the literature, however, many of the experimental data such as the stoichiometric flow ratio or the exact cell geometry and dimensions are unknown, which makes a quantitative comparison difficult. The strength of the current model is clearly to perform parametric studies and explore the impact of various parameters on the transport mechanisms and on fuel cell performance.

For the binary diffusivities D_{ij} required in the Stefan–Maxwell equations, experimentally obtained values at atmospheric pressure p_0 were taken and scaled with the temperature and pressure according to [6]

$$D_{ij} = D_{ij}(T_0, p_0)\,\frac{p}{p_0}\left(\frac{T}{T_0}\right)^{1.5} \tag{47}$$

Table 2 lists the reference binary diffusivities.

Table 2
Binary diffusivities at reference temperatures

Gas-pair	Reference temperature, T_0 (K)	Binary diffusivity, D_{ij} (cm^2/s)
$D_{H_2-H_2O}$	307.1	0.915
$D_{H_2-CO_2}$	298.0	0.646
$D_{H_2O-CO_2}$	307.5	0.202
$D_{O_2-H_2O}$	308.1	0.282
$D_{O_2-N_2}$	293.2	0.220
$D_{H_2O-N_2}$	307.5	0.256

3. Results and discussion

3.1. Fuel cell performance

The fuel cell performance is shown in terms of the polarization in Fig. 4. The results agree well with the experiments [17] in the low and intermediate current density region. The discrepancy at high current densities is attributed to the fact that experimental data at the higher current densities was insufficient, and in fact the experimental curve in this region is a curve fit weighted by the lower current density data. It should also be pointed out that the exact geometry of the fuel cell used in the experiments is not known. The ability of the present model to reproduce the polarization curve is a necessary validation check but by no means especially informative since one can always obtain good agreement between experimental results and any model that somehow captures the logarithmic drop-off in the low current density region and the Ohmic losses inside the membrane. The strength of the numerical approach is in providing detailed insight into the various transport mechanisms and their interaction, and in the possibility of performing parameters sensitivity analyses.

3.2. Reactant gas and temperature distribution

One of the major advantages of using a model as detailed as the one presented here is the detailed distribution of the reactant gases inside the fuel cell. Such distributions, which cannot be measured in situ, provide valuable information about the onset of concentration losses and their effect on the limiting current density. Fig. 5 shows the reactant gas distribution in the fuel cell channels and the gas-diffusion layers. The molar fraction of oxygen decreases noticeable inside the gas-diffusion layer, and the effect of oxygen depletion is significant, particularly under the land areas. A realistic prediction of the limiting current density cannot be obtained from a two-dimensional model in which infinitely wide channels are assumed and the area that is not exposed to the gas-flow channels is not accounted for.

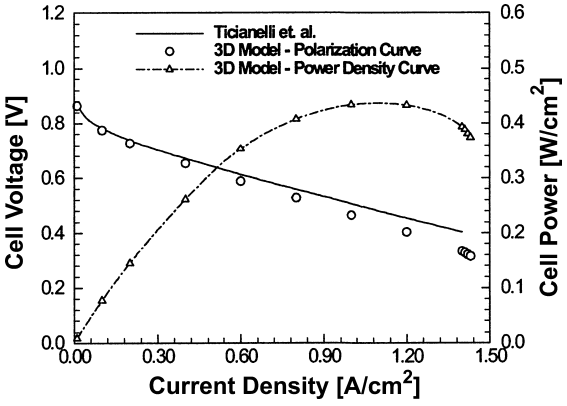

Fig. 4. Comparison of the experimental and simulated polarization curves. Also shown is the power density curve obtained with the model.

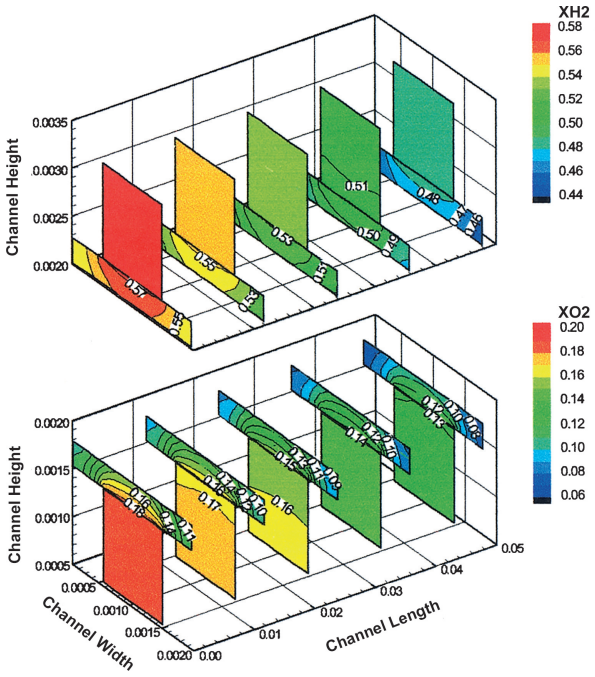

Fig. 5. Three-dimensional distribution of reactant gases in the gas-flow

The effect of the ''land area'' is even more pronounced at higher current densities, as shown in Fig. 6. Furthermore, for a higher current density at otherwise similar conditions, the oxygen molar fraction at the catalyst layer decreases due to diffusion limitations. Note that the stoichiometric flow ratio is the same for both cases, i.e. three times the amount of oxygen consumed enters the cell. Since the composition of

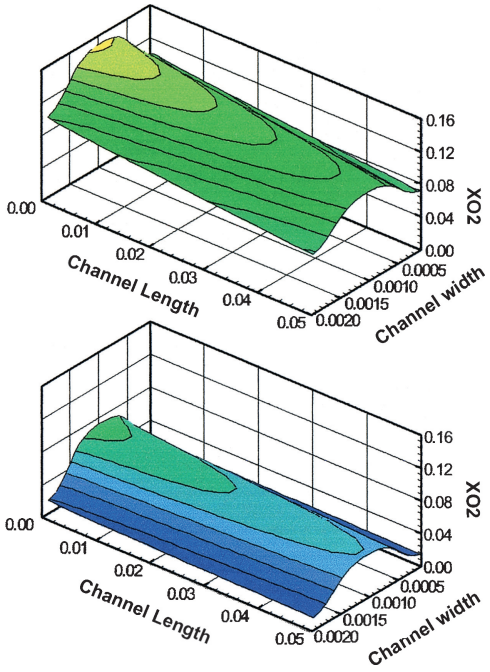

Fig. 6. Molar oxygen fraction at the catalyst layer for two different current densities: 0.2 A/cm^2 (upper) and 1.0 A/cm^2 (lower).

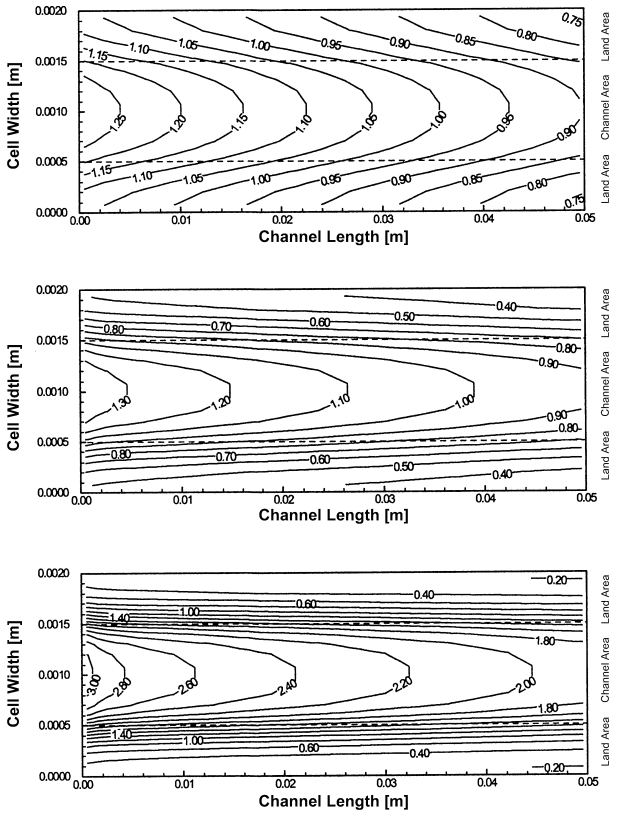

Fig. 7. Dimensionless current density distribution at the catalyst layer interface for three different nominal current densities: 0.2 A/cm^2 (upper); 0.8 A/cm^2 (middle); 1.4 A/cm^2 (lower). The dashed lines represent the boundaries between the flow channel and the land area.

the inlet gases is the same, this is accomplished by an increase in velocity for a higher current density. At an average current density of 1.4 A/cm^2, the molar oxygen fraction at the catalyst layer is almost zero throughout the interface, indicating that the limiting current density has been reached.

The detailed oxygen distribution at the catalyst layer is of importance, because it determines the local current density, according to Eq. (29). Assuming a constant activation overpotential throughout the catalyst interface, this results in local current densities as shown in Fig. 7. The local current densities here have been normalized by the nominal current density in each case. It can be seen that for a low nominal current density, the distribution is quite uniform with variations from 75 to 125% relative to the nominal current density of 0.2 A/cm^2. This changes for intermediate current densities, where under the land areas a noticeable decrease takes place and the minimum current fraction drops below 40% of the average (nominal) current density of 0.8 A/cm^2. The maximum, however, remains almost the same at just over 130%. This pattern changes further at high current densities, where the maximum local current density can be as high as three times the average current density near the cathode side inlet.

With an increase in current density, the fraction of the current density generated under the area exposed to the

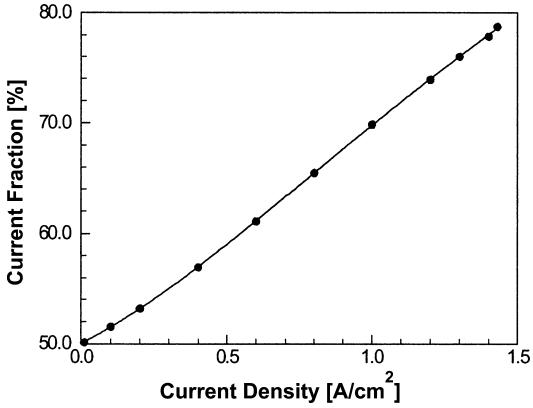

Fig. 8. Fraction of the total current generated under the area exposed to the gas-flow channels.

gas-flow channels increases steadily, as shown in Fig. 8. The fraction of the current generated under the channel area increases almost linearly with the current density, the maximum being just under 80% at a current density close to the limiting current density. This is important, since it provides an indication of how well the catalyst is being used in these areas. For optimal fuel cell performance, a uniform current density generation is desirable, and this could only be achieved with a non-uniform catalyst distribution, possibly in conjunction with non-homogeneous GDEs.

One of the most important features distinguishing the present model is the fact that it is non-isothermal. The temperature distribution inside the fuel cell has important effects on nearly all transport phenomena, and knowledge of the magnitude of temperature increases due to irreversibilities might help preventing failure. Fig. 9 shows that the increase in temperature can exceed several degrees Kelvin near the inlet area, where the local current density is highest. Due to the low electric conductivity of the polymer electrolyte, the temperature maximum occurs inside the membrane. In general, the temperature at the cathode side is slightly higher than at the anode side; this is due to the reversible and irreversible entropy production. The detailed temperature distribution is also key for the eventual extension of the current model to include multiphase phenomena. Phase change is not yet accounted for, but the mechanism shall be briefly outlined here. In the first place, the temperature rise at the cathode determines, how strong the under-saturation of the gas phase in this area is. This in turn gives rise to the evaporation of liquid product water, which provides cooling and thus offsets the temperature rise. Hence, any implementation of phase change in an isothermal model can not lead to physically representative results.

Finally, the water flux and the potential distribution is presented in Fig. 10. The flux of liquid water is governed by three mechanisms: electro-osmotic drag from the anode to the cathode, back diffusion driven by a concentration gradient from the cathode to the anode and, if a pressure gradient exists, convection which is usually directed from the cathode to the anode in order to counter-balance the

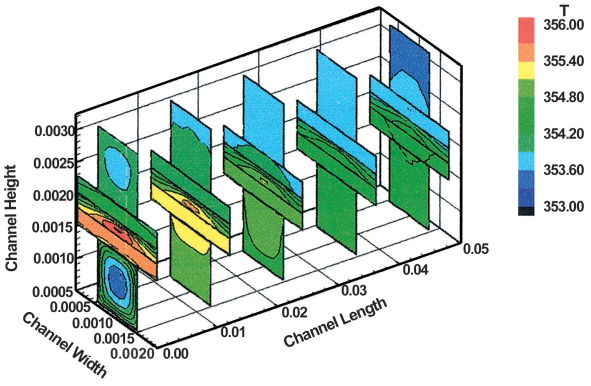

Fig. 9. Three-dimensional temperature distribution inside the fuel cell at a nominal current density of 1.2 A/cm^2.

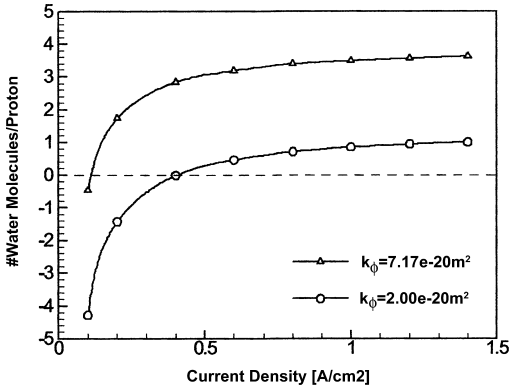

Fig. 11. Net drag coefficient α for the flux of water through the membrane for two different values of the electrokinetic permeability of the membrane.

electro-osmotic drag. Assuming a fully humidified membrane implies no concentration gradient exists, and in any case, the effect of the diffusion on the water flux through the membrane has been found to be small compared to convection and electro-osmotic drag. As illustrated in Fig. 10, the pressure gradient might outweigh the effect of the electro-osmotic drag for low current densities, and the net flux of water is directed from the cathode to the anode. Humidification schemes have to be therefore devised for the cathode side only. At a current density of 0.4 A/cm^2, the flux of water is reversed. Near the inlet area, where the local current is strongest, the electro-osmotic drag dominates convection, and water flows from the anode to the cathode. Near the outlet, the current is weaker and the net water flux is directed towards the anode.

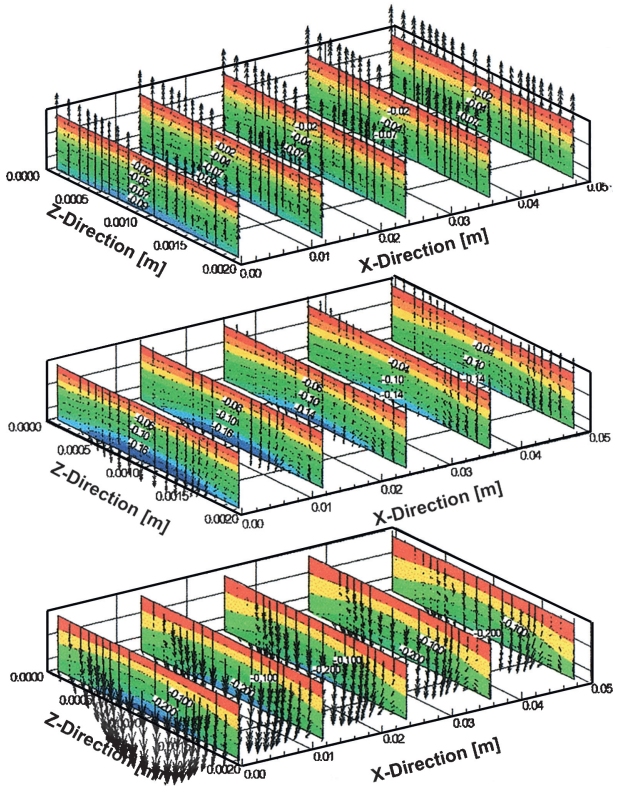

Fig. 10. Liquid water flux (vectors) and potential distribution (contours) inside the membrane for three different current densities: 0.2 A/cm^2 (upper); 0.4 A/cm^2 (middle); 0.6 A/cm^2 (lower).

The net flux of water through the membrane is often characterized by the parameter α, the net amount of water molecules dragged through the membrane per hydrogen proton. Fig. 11 shows the net water flux for two different values of the electrokinetic permeability of the membrane. If the value cited by Bernardi and Verbrugge is used [4], α becomes unphysically high. A comparison with the model published by Yi and Nguyen [21] reveals that reducing the permeability to 2.0×10^{-20} m^2 as was used in the current base case yields a more realistic values for α. Still, these results differ substantially from the experimentally determined values of α, which range from 0.6 at low current densities to around 0.3 for intermediate current densities in the absence of a pressure gradient. The membrane model has therefore to be improved in order to predict the amount of water that need to be supplied at the electrodes in order to prevent drying out of the membrane.

4. Conclusions

A comprehensive three-dimensional computational model of a PEM fuel cell has been developed. With the exception of phase change, the model accounts for all major transport phenomena in the flow channels, electrodes and electrolyte membrane. Results that are physically consistent and in good agreement with available experimental data are obtained. The three-dimensional nature of the distribution of flow velocities, species concentration, mass transfer rates, electric current and temperature was clearly illustrated by the simulations. The capabilities of the model for providing detailed insight into water transport mechanisms and the onset of mass transport limitations was demonstrated, and its potential for parametric studies of interest in design and prototyping were also illustrated.

Though this comprehensive model represents to our knowledge the only three-dimensional model developed to date, a number of important mechanisms and phenomena need to be incorporated to increase its generality and usefulness. Work is currently in progress to account for (a) the effect of phase change of water, and (b) partial dehydration of the membrane during operation. Finally the electrochemistry in the computational model relies on first order kinetics and empirical data. Further work in this area is required on both theoretical and experimental fronts.

References

[1] A.J. Bard, L.R. Faulkner, Electrochemical Methods, Wiley, New York, 1980.
[2] J.J. Baschuk, X. Li, Modelling of polymer electrolyte membrane fuel cells with variable degrees of water flooding, J. Power Sources 86 (2000) 181–195.
[3] D.M. Bernardi, M.W. Verbrugge, Mathematical model of a gas diffusion electrode bonded to a polymer electrolyte, AIChE J. 37 (8) (1992) 1151–1163.
[4] D.M. Bernardi, M.W. Verbrugge, A mathematical model of the solid-polymer-electrolyte fuel cell, J. Electrochem. Soc. 139 (9) (1992) 2477–2491.
[5] J. O'M Bockris, S. Srinivasan, Fuel Cells: Their Electrochemistry, McGraw-Hill, New York, 1969.
[6] E.L. Cussler, Diffusion–Mass Transfer in Fluid Systems, Cambridge University Press, Cambridge, 1984.
[7] N. Djilali, D.M. Lu, Influence of heat transfer on gas and water transport in fuel cells, Int. J. Thermal Sci., in print, 2002.
[8] T.F. Fuller, J. Newman, Water and thermal managament in solid-polymer-electrolyte fuel cells, J. Electrochem. Soc. 140 (5) (1993) 1218–1225.
[9] V. Gurau, H. Liu, S. Kakac, Two-dimensional model for proton exchange membrane fuel cells, AIChE J. 44 (11) (1998) 2410–2422.
[10] F.P. Incropera, D.P. DeWitt, Fundamentals of Heat and Mass Transfer, 4th Edition, Wiley, New York, 1996.
[11] M.J. Lampinen, M. Fomino, Analysis of free energy and entropy changes for half-cell reactions, J. Electrochem. Soc.140 (12) (1993) 3537–3546.
[12] T.V. Nguyen, R.E. White, A water and heat management model for proton-exchange-membrane fuel cells, J. Electrochem. Soc. 140 (8) (1993) 2178–2186.
[13] A. Parthasarathi, S. Srinivasen, J.A. Appleby, C.R. Martin, Temperature dependance of electrode kinetics of oxygen reduction at the Platinum/Nafion interface—A microelectronic investigation, J. Electrochem. Soc. 139 (9) (1992) 2530–2537.
[14] T.E. Springer, T.A. Zawodzinski, S. Gottesfeld, Polymer electrolyte fuel cell model, J. Electrochem. Soc.138 (8) (1991) 2334–2342.
[15] R. Taylor, R. Krishna, Multicomponent Mass Transfer, Wiley, New York, 1993.
[16] E.A. Ticianelli, J.G. Berry, S. Srinivasan, Dependence of performance of solid polymer electrolyte fuedl cells with low platinum loading on morphologic characteristics of the electrodes, J. Electroanal. Chem. 251 (1988) 275–295.
[17] E.A. Ticianelli, C.R. Derouin, A. Redondo, S. Srinivasan, Methods to advance technology of proton exchange membrane fuel cells, J. Electrochem. Soc.135 (9) (1988) 2209–2214.
[18] S. Um, C.Y. Wang, K.S. Chen, Computational fluid dynamics modeling of proton exchange membrane fuel cells, J. Electrochem. Soc. 147 (12) (2000) 4485–4493.
[19] Z.H. Wang, C.Y. Wang, K.S. Chen, Two-phase flow and transport in the air cathode of proton exchange membrane fuel cells, J. Power Sources 94 (2001) 40–50.
[20] M. Woehr, K. Bolwin, W. Schnurnberger, M. Fischer, W. Neubrand, G. Eigenberger, Dynamic modelling and simulation of a polymer membrane fuel cell includinmg mass transport limitations, Int. J. Hydrogen Energy 23 (3) (1998) 213–218.
[21] J.S. Yi, T.V. Nguyen, An along-the-channel model for proton exchange membrane fuel cells, J. Electrochem. Soc. 145 (4) (1998) 1149–1159.